HHS Public Access

Author manuscript

Magn Reson Med. Author manuscript; available in PMC 2017 March 01.

Published in final edited form as:

Magn Reson Med. 2016 March ; 75(3): 1346–1354. doi:10.1002/mrm.25558.

Accelerated and motion-robust in vivo T_2 mapping from radially undersampled data using Bloch-simulation-based iterative reconstruction

Noam Ben-Eliezer[1], **Daniel K Sodickson**[1], **Timothy Shepherd**[1], **Graham C Wiggins**[1], and **Kai Tobias Block**[1]

[1] The Bernard and Irene Schwartz Center for Biomedical Imaging, Department of Radiology, New York University School of Medicine, New York, NY 10016, USA

Abstract

Purpose—Development of a quantitative T_2-mapping platform that operates at clinically feasible timescales by employing advanced image-reconstruction of radially undersampled multi spin-echo (**MSE**) datasets.

Methods—Data was acquired on phantom and in vivo at 3 Tesla using MSE protocols employing radial k-space sampling trajectories. In order to overcome the non-trivial spin evolution associated with MSE protocols a numerical signal model was pre-calculated based on Bloch simulations of the actual pulse-sequence scheme used in the acquisition process. This signal model was subsequently incorporated into an iterative model-based image reconstruction process, producing a T_2 and proton-density maps.

Results—T_2 maps of phantom and in vivo brain were successfully constructed, closely matching values produced by a single spin-echo reference scan. High-resolution mapping was also performed for the spinal cord in vivo, differentiating the underlying gray/white matter morphology.

Conclusion—The presented MSE data processing framework offers reliable mapping of T_2 relaxation values in a ~5 minutes timescale, free of user- and scanner-dependent variations. The use of radial k-space sampling provides further advantages in the form of high immunity to irregular physiological motion, as well as enhanced spatial resolutions owing to its inherent ability to perform alias-free limited field-of-view imaging.

Keywords

Quantitative MRI; T_2 mapping; Model-Based Reconstruction; Radial k-space sampling

INTRODUCTION

Quantitative mapping of the transverse relaxation time ($\mathbf{T_2}$) in magnetic resonance imaging can be used to detect pathological tissue changes in various clinical and research applications, including diagnosis of brain ischemic stroke [1], assessment of cognitive

Corresponding author: Ben-Eliezer Noam Telephone: +1-212-263-4858 Noam.Ben-Eliezer@nyumc.org.

impairment in multiple sclerosis [2], identification of cardiac edema and iron overload [3-5], cancer detection [6,7], and musculoskeletal imaging [8,9]. Despite its potentially high impact, the estimation of T_2 values in vivo remains highly challenging, owing to the large number of spatial and temporal data-points that need to be sampled in order to construct high-quality maps. The use of traditional single spin-echo (**SE**) imaging protocols is impractical for in vivo imaging due to their prolonged scan times (10s of minutes), which compromise patient throughput and lead to strong motion artifacts. A more realistic alternative is provided by multi-SE (**MSE**) protocols, which collect data at a series of distinct echo times (**TE**) during each repetition time (**TR**), thereby significantly shortening the overall scan time. An even higher efficiency can be achieved by sampling k-space radially, offering lower motion sensitivity [10], and, as will be later seen, higher efficiency when scanning small structures owing to its ability to acquire partial FOVs, requiring smaller matrix sizes for a given target resolution. Its intrinsically incoherent undersampling artifacts, can be further utilized for accelerating the acquisition either by employing compressed sensing (CS) [11,12] or using an inverse-problem formulation with analytical modeling of the acquired signal in the data reconstruction process [13]. The advantages of radial MSE protocols, however, are offset by the complexity of reconstructing the desired image-space maps, particularly when dealing with undersampled data. Another major complication is the inherent bias of MSE signal due to stimulated and indirect echoes, non-rectangular slice profiles, and transmit ($\mathbf{B}^{+}_{\mathbf{1}}$) field inhomogeneities. These cause the T_2 decay profile to deviate from the theoretical exponential model $S(t)=S_0\exp(-t/T_2)$, leading to significant T_2 estimation errors, which moreover vary between scanners and protocol versions due to practical differences between the corresponding pulse sequence implementation and experimental parameters.

A variety of approaches have been described for reconstructing undersampled radial MSE datasets. These are typically based on iterative processes which involve interpolation of the k-space data onto a Cartesian grid and fitting the temporal-domain data to a simplified model of the MSE T_2 decay curve [14-16]. More advanced approaches exist, such as the CURLIE algorithm [17], which employs the slice-resolved EPG algorithm [18] to obtain more realistic decay curves for a model-based reconstruction of radially sampled datasets. The non-linearity that is inherent to this type of reconstruction originates from the fact that the signal model incorporates the target maps via a non-linear operation, and is handled via PCA based linearization of the T_2 relaxation effect in MSE protocols. A recent report introduced the echo-modulation curve (**EMC**) T_2 mapping technique [19], which models the non-exponential T_2 decay curve through Bloch simulations that are tailored to the specific pulse sequence being employed, rather than rely on the generic EPG model. This work presents first results of using the EMC algorithm in a model-based iterative reconstruction of radially sampled data. The generalized EMC-based signal model is designed to accurately reflect the pulse sequence scheme and parameter values, including the slice profile, RF pulse shapes, crusher gradients, and the effect of spin relaxation during the RF pulses – a highly significant factor in light of the non-negligible duration of the refocusing pulses with respect to the echo train length. The ensuing reconstruction procedure offers fast and reliable quantification of proton density (**PD**) and T_2 relaxation values in clinically feasible

timescales. Validations are presented using phantoms, in vivo brain data as well as high-resolution mapping of the gray / white matter in the spinal cord.

METHODS

Theoretical formalism of iterative EMC-based reconstruction

A detailed description of the principles underlying traditional iterative model-based reconstruction of radially sampled data can be found in [13]. In essence, it is based on modeling the k-space signal using a forward acquisition operator given by

$$F_{t,c,j}(\rho, T_2) = \sum_{\vec{r} \in FOV} \rho(\vec{r}) \cdot e^{-t/T_2(\vec{r})} \cdot C_c(\vec{r}) \cdot e^{-i\vec{k}_j \cdot \vec{r}} \quad (1)$$

where t denotes the echo-time (**TE**) taking any discrete value determined by the sequence, j is an index into the set of consecutive signal-points acquired during each radial readout event $\bar{k}_j = [k_x, k_y]_j$, $\vec{r}$ denotes an image-space position $\vec{r} = [r_x, r_y]$, and C_c is the complex sensitivity profile of the c^{th} coil. The resulting operator F represents a single readout event and reflects the sequential application of T_2 relaxation, coil sensitivity, and gradient-encoding operators on the proton density ρ. The unknowns being sought for are the spatial distributions of T_2 and ρ, denoting the spin-spin relaxation and the spin-density, respectively. Computation of the maps is performed using numerical minimization of a cost function, Φ, which evaluates the consistency of the T_2 and ρ parametric maps with respect to the raw k-space data

$$\Phi(\rho, T_2) = \frac{1}{2}\sum_t \sum_c \left\| \left(\vec{F}_{t,c} - \vec{y}_{t,c} \right) \right\|_2^2 = \Phi(\rho, T_2) = \frac{1}{2}\sum_t \sum_c \sum_j (F_{t,c,j} - y_{t,c,j})^2 \quad (2)$$

The indices t and c run over the entire set of echo times and receive channels, while y represents the acquired k-space signal of a single readout event, detected in channel c, and at echo time t.

The relaxation model embedded in Eq. (1) reflects a purely exponential decay that breaks down for MSE pulse sequences on account of stimulated and indirect coherence pathways. These lead to significant errors, ranging up to as much as 50% to 100% of the true T_2 values when signal decay curves are fitted to a simple exponential [19]. More accurate predictions can be obtained using customized acquisition schemes [20,21], tailored analytical signal models [22], or using algorithms that take into account the various factors that affect the spin dynamics in MSE sequences [18,23]. In order to be compatible with the minimization of Eq. (2), any signal-model needs furthermore to be well-defined and derivable throughout the parameter search space. Our implementation uses the numerical EMC algorithm described in reference [19], offering comprehensive modeling of MSE protocols based on computer simulations of the time-dependent Bloch equations for the actual MSE pulse sequence executed on the scanner. These simulations incorporate the exact RF pulse shapes, gradient waveforms, and other parameters to generate an estimated echo-modulation curve for a given pulse sequence scheme and set of experimental parameter values. Simulations are repeated for a range of T_2 and B^+_1 values, ultimately generating a database of EMCs,

each associated with a unique [B^{+}_{1},T_2] value pair. The choice of considering the transmit-field as an unknown in the fitting process stems from the relatively high variability of the B^{+}_{1} field around the prescribed flip-angle, a factor which is further accentuated owing to the typically large number of refocusing RF pulses applied in MSE protocols. Various other parameters, such as the echo spacing, acquisition duration and bandwidth, and crusher gradient timings and moments, also affect the final decay curve. The value of these parameters can be accurately extracted from the vendor's pulse-program scheme and then used as an input to the simulation process. The role of T_1 relaxation has also been investigated in the context of the EMC algorithm, and in agreement with previous reports [18,22,24], was found to have very little effect on the experimental echo-modulation curve. It was therefore set to a fixed value of 0.5 sec for the phantom measurements and to 1 sec for the in vivo scans.

Updating Eq. (1) with an MSE-adapted relaxation term generated by the EMC algorithm yields

$$F_{t,c,j}(\rho,T_2)=\sum_{\vec{r}\in FOV}\rho(\vec{r})\cdot EMC(B_1(\vec{r}),T_2(\vec{r}),t)\cdot C_c(\vec{r})\cdot e^{-i\vec{k}_j\cdot\vec{r}} \quad (3)$$

A second step in integrating the EMC algorithm into the CG iterative reconstruction is to define derivatives of the cost function Φ in Eq. (2) with respect to the values of the three unknowns (ρ, T_2 and B_1^{+}) at each spatial location. A derivative with respect to an arbitrary variable ξ will have the form [13]

$$\frac{\partial\Phi}{\partial\xi}=\frac{1}{2}\sum_t\sum_c\frac{\partial}{\partial\xi}\left[\sum_j(F_{t,c,j}-y_{t,c,j})\overline{(F_{t,c,j}-y_{t,c,j})}\right]=\sum_t\sum_c\left[\Re\left\{\sum_j(F_{t,c,j}-y_{t,c,j})\frac{\partial}{\partial\xi}\overline{F_{t,c,j}}\right\}\right]; \quad (4)$$

where $\overline{(\cdot)}$ denoted the complex conjugate, and $\Re\{\cdot\}$ is the real value. This reduces the problem to deriving *F* with respect to the ρ, T_2 and B^{+}_{1} map values at each pixel. Inserting Eq. (3) into this expression we obtain

$$\frac{\partial\Phi}{\partial\rho_\upsilon}=\sum_t\sum_c EMC\left(B^{+}_{1,\upsilon},T_{2,\upsilon},t\right)\cdot\underbrace{\Re\left\{\overline{C_c(\vec{r}_\upsilon)}\cdot\sum_j(F_{t,c,j}-y_{t,c,j})e^{+i\vec{k}_j\cdot\vec{r}_\upsilon}\right\}}_{\equiv\mathrm{Y}} \quad (5)$$

$$\frac{\partial\Phi}{\partial T_{2,\upsilon}}=\sum_t\sum_c\left[\frac{\partial EMC\left(B^{+}_{1,\upsilon},T_{2,\upsilon},t\right)}{\partial T_{2,\upsilon}}\right]\cdot\rho(\vec{r}_\upsilon)\cdot\mathrm{Y} \quad (6)$$

$$\frac{\partial\Phi}{\partial B_{1,\upsilon}}=\sum_t\sum_c\left[\frac{\partial EMC\left(B^{+}_{1,\upsilon},T_{2,\upsilon},t\right)}{\partial B_{1,\upsilon}}\right]\cdot\rho(\vec{r}_\upsilon)\cdot\mathrm{Y} \quad (7)$$

where υ is a voxel index running over the entire maps' FOV.

The derivatives of the EMC term in Eqs. (6)-(7) were calculated numerically and are described in Appendix A. In practice, we found that higher T2-maps' accuracy is achieved by interpolating the numerical EMC database with respect to the discrete T_2 parameter. This is particularly valuable for data with short T_2 values where non-negligible difference exists between echo-modulation curves of neighboring T_2 values. Using straightforward linear interpolation, the gap between each two simulated EMCs corresponding to neighboring T_2 values, was populated with estimated EMCs to produce higher level of discretization. A 5-fold linear interpolation was used to increase the database discretization from ΔT_2=1 ms to ΔT_2=0.2 ms, and found to be sufficient for post-processing of all datasets.

Regularization

Notwithstanding the motion robustness entailed by radial sampling, phase inconsistencies, and partial voluming effects can still result from irregular patient- or physiological-related motion, occurring for example in the prostate or spinal cord, and translating into reconstruction noise. Several regularization strategies were investigated in this context, the most effective of which was the addition of Tikhonov regularization terms to the cost function with separate λ_i weighting for each of the fitted maps

$$\Phi(\rho,T_2)=\frac{1}{2}\left(\sum_t\sum_c\left\|\sum_j\left(F_{t,c,j}-y_{t,c,j}\right)\right\|_2^2+\lambda_\rho\left\|\sum_{\vec{r}\in ROI}\rho(\vec{r})\right\|_2^2+\lambda_T\left\|\sum_{\vec{r}\in ROI}T_2(\vec{r})\right\|_2^2+\lambda_B\left\|\sum_{\vec{r}\in ROI}\tilde{B}_1^+(\vec{r})\right\|_2^2\right) \quad (8)$$

The derivatives of the new terms are straightforward and simply proportional to the map values themselves. Apart from improving the reconstruction stability [25], the use of spatially-specific regularization, offered a convenient mechanism for imposing spatial smoothness on the B^+_1 map which is expected to have slowly varying features. This was achieved by using a modified B_1^+ map (denoted by $\tilde{B}_1^+$), equal to the original map minus its mean value. The iterative process thus acts so as to minimize the B^+_1 variation around a certain baseline, better matching the physical system at hand. Further practical aspects pertaining to the regularization terms can be found in Appendix B.

Data acquisition

Experiments were performed on a 3 T whole-body MR system (MAGNTOM Trio, Siemens AG Healthcare, Erlangen, Germany) for T_2 phantoms as well as human subjects. The experimental protocol involved running a radial MSE protocol (which constitutes the focus of this work) and two reference protocols: Cartesian MSE and Cartesian single-SE protocols. The radial protocol consisted of $\mathbf{N_{EXC}}$ spin excitations (one per TR) applying a 90° slice-selective RF pulse, followed by a train of ETL spin-echo readouts. Each of these readouts acquired a single spoke at a unique angular orientation. Refocusing pulses were enclosed by crusher gradients in order to dephase spurious FID signals. The angular increment between each spoke (within an echo train as well as between consecutive echo trains) was fixed at the golden-angle (~111.246°), generating a non-repeating set of spoke angles. A key consideration in employing such a sampling scheme for mapping T_2 relaxation is the need to homogeneously cover the object's k-space, separately for each of the echo times used. Since not every choice of [N_{EXC},ETL] values meets this condition, an

allowed set of value-pairs was determined via computer simulations of the k-space coverage per TE in the relevant parameter range. Reference T_2 values were generated from a Cartesian MSE protocol, sampling each k-space line multiple times following a 90° slice-selective excitation producing a series of 2D images that correspond to increasing TEs. A second reference was collected where applicable (i.e. when scan times were not prohibitive), using a full single-SE protocol, providing a more definitive map of the object's T_2 values.

Phantom scans were performed using a 12-element head coil array for data reception. Excitation was performed with the scanner's built-in body coil. The phantom is shown in Figure 1 and consists of a matrix of nine 15 ml plastic tubes containing purified water doped with $MnCl_2$ concentrations of 0.070, 0.135, 0.270, 0.405, 0.540, 0.675, 0.800, 1.000, and 0.540 mM (corresponding to the tube numbers 1 through 9). Tubes #5 and #9 were deliberately filled with identical concentrations in order to test spatial variation of the parameter extraction. This phantom offered a broad range of T_2 values with an average T_1/T_2 ratio of 13.8 ± 1.3, similar to human tissues [20,26]. T_1 values were estimated using a double-flip-angle T_1 weighted 3D gradient echo protocol provided by the vendor. Phantom scans were repeated for refocusing angles 180°, 150°, 120°, and 90° in order to assess the mapping stability over a range of commonly used values. Experimental parameters' values for all scans are summarized in Table 1. Similar scan times were chosen for the Cartesian and radial MSE protocols in order to be able – particularly in the in vivo scans – to compare the accuracy and efficiency of the two acquisition schemes under similar experimental conditions (see the Discussion for more details).

In vivo validations were performed for the brain (N=5) and cervical spinal-cord (N=5) of healthy volunteers under institutional IRB guidelines and after obtaining written informed consent. Brain scans were performed with a receive-only 12-element head coil array, while the cervical spinal-cord scans were performed using a custom-built receive-only 8-element neck coil array. Parameters' values for all scans are delineated in Table 1. Single-SE data were not collected during the spinal-cord scans due to severe artifacts caused by CSF pulsation as well as cardiac and respiratory motion. Partial alleviation of the physiologic motion associated with cardiac pulsation was achieved by triggering the acquisition using a pulse-oximeter attached to the index finger of each volunteer, using a 10ms delay after the mid-systolic time point [27]. Acceleration was not applied in the Cartesian spinal cord scan due to the appearance of residual artifacts attributed to the GRAPPA reconstruction of such small ROIs.

Reconstruction

Post-processing of the radial MSE data was performed using an in-house software package written in C/C++. As a preliminary step, the coil sensitivity profiles were estimated from the raw data according to procedure described in [28]. T_2 and PD maps were generated by executing the non-linear CG algorithm described in [29] using the objective function in Eq. (8). For the interpolation in k-space from a Cartesian grid to radial spokes and vice versa, a Kaiser-Bessel window with $L = 5$ and $\beta = 7.33$ was used, while utilizing the default two-fold oversampling factor of the raw data exported from the scanner [30]. The stability and convergence of CG algorithms are typically sensitive to the relative scaling between the

fitted parameters [13,16]. This results from the intrinsically different baseline value of the PD, T_2 and B_1^+ maps. Improper scaling thus leads to disproportionate step sizes for the various parameters and may even cause divergence of the iterative process. Suitable tuning of the map values was achieved by scaling down the T_2 time axis by a factor of 250 and the B_1^+ map values by a factor of 2000. The optimal downscaling factor was found by examining the L_2-norm of the *gradient* of each map (Eq. (5)-(7)) during execution of the iterative process, and setting the corresponding scaling factors so as to keep the relative gradients of the T_2 and B_1^+ maps in the range of 10% ... 20% of the PD map gradient value. Tikhonov regularization of the PD and B_1^+ maps was incorporated into all data post-processing employing [λ_ρ=1, λ_T=0, λ_B =10]. The CG process converged after 200 or more iterations for the phantom and brain data, and at 150...200 iterations for the spinal-cord data, after which noise-amplification artifacts emerged for low SNR regions. As a last practical step, the CG-reconstruction process was restarted every N=20 iterations where the result of the n^{th} run was used as an input for the n^{th}+1 run. Since during each execution, the CG-descent algorithm avoids repeating the same search directions in the parameter-space more than once, restarting the process allowed previous search directions to become available [31]. This is a desired feature in light of the non-linearity of the model being fitted, and yielded faster and more reliable convergence.

T_2 maps were also generated from the single-SE and multi-SE Cartesian data. The single-SE data was processed by fitting each pixel in the corresponding time-series of DICOM images to an exponential decay of the form $S(t)=S_0\exp(-t/T_2)$. Although the resulting maps may be affected by residual diffusion bias, this effect is negligible in comparison to the variability of the T_2 values in vivo [32], and the maps were therefore used in this study as a baseline reference for the MSE maps. Cartesian MSE data was processed according to the EMC algorithm described in [19]. In essence, the algorithm relies on matching the series of DICOM images to a pre-calculated database of simulated EMCs. This database is constructed numerically using Bloch-simulations of the pulse sequence scheme, and incorporates the exact protocol's experimental parameter-values, RF shapes, gradient waveforms, and event timing. Further information, including the source code of the simulations described in this report, the iterative model-based reconstruction code, as well as an EMC based graphical-user-interface (GUI) for reconstructing T_2 maps is available online at [33]. Computation time was approximately 1 minute for a matrix of 128x128 pixels using a standard desktop computer. This procedure resulted in assigning a unique T_2 value to each pixel, yielding the final T_2 map. As a second step, PD maps were calculated for both single-SE and MSE data by taking the T_2 weighted image of the first TE, and extrapolating it to time t=0 by dividing each pixel in the image by its T_2 decay factor $\exp(-TE/T_2)$ predicted by the T_2 map.

RESULTS

$MnCl_2$ phantom scans

Table 2 summarizes the measured T_2 values for the nine-tube phantom shown in Figure 1. Good correlation exists between the single-SE data and the radial MSE data (average p-value < 1e-9). Fitting accuracy is furthermore relatively stable over the range of T_2 values

and for refocusing flip-angles down to 90°. Considering the single-SE values as the ground truth, slightly higher overall accuracy is achieved by the Cartesian MSE T_2 mapping protocol for all refocusing flip angles assayed. This result is expected given the complexity of radial sampling and reconstruction compared to the Cartesian approach, and the ideal conditions of scanning a phantom, where the improved motion robustness of radial trajectories is not manifested. A significant overestimation of the T_2 values emerges when using straightforward mono-exponential fit to process MSE data (rightmost four columns). This results from not accounting for stimulated and indirect echoes, which cause artificial elongation of the later parts of the echo train. The effect is further amplified when shifting from an optimal 180° refocusing flip angle as a higher percentage of the signal is then dominated by indirect echoes.

In vivo scans

Figure 2 compares representative T_2 and PD maps of the human brain produced from Cartesian single-SE, Cartesian MSE and radial MSE data. Very good correlation is observed between all three data sets with the MSE protocols providing higher spatial resolutions owing to the extensive scan times that would have been required in order to achieve similar resolution using a single-SE protocol. CSF pulsation occurring over the 22-minute-long scan still affects the single-SE maps and manifests as residual artifacts within the ventricles. Apart from the excellent match to the reference Cartesian data, the radially sampled maps also offer slightly higher definition and better coverage of the peripheral scalp area, a result which can be ascribed to its higher robustness to physiological motion.

The potential advantages of radial sampling are further illustrated in Figure 3, showing T_2 and PD maps of an axial slice at the C3 vertebrae of the cervical spinal cord (slice location shown in panel 3e). The small features of this anatomy pose a considerable challenge for T_2 mapping, which is moreover exacerbated by in-plane CSF pulsations and through-plane flow. Panels 3b,d demonstrate the ability of radial sampling to alleviate these motion-related artifacts and extract high resolution anatomical information, clearly differentiating the gray and white matter tracts within the spinal cord. Slight blurring appears in the peripheral parts of these maps as a result of excluding these regions from the spatial-domain regularization terms in (8) in order to achieve faster convergence at the region-of-interest (see Methods Section). A corresponding set of Cartesian sampled maps, acquired during the same scan session and using identical parameters, are shown in Panels 3a,c. Although the Cartesian PD map exhibits the same general morphology as the radial map, this data is strongly affected by motion, and fails to produce consistent T_2 maps, or extract the internal features of the cord. Quantitative measurements on the segmented ROIs in Panel 3b produced mean T_2 values equal to 58.9 ± 4.0 ms for white matter and 71.4 ± 12.6 ms for gray matter. Although the lack of gold standard measurements for the spinal cord prevents conclusive validation of these values, a close match exists between the gray matter T_2 value and previously reported value of 73 ± 3 ms [27]. Further corroborations are provided by the T_2 values of the surrounding muscle tissue (31.8 ± 0.3 ms) which match values reported in the literature [34,35], and by the good correspondence of the gray/white matter T_2 ratio (~1.2) to similar values reported for brain tissues [36,37].

DISCUSSION

The EMC algorithm offers fast and accurate mapping of tissue T_2 and PD values, independent of the specific scanner type and pulse sequence implementation. Its combination with radial sampling offers improved immunity to physiological and patient motion and, owing to the inherent multidimensional readout-oversampling of this acquisition scheme, allows scanning partial field-of-views at arbitrary spatial resolutions, thereby further shortening scan times. Although this report does not fully explore the acceleration potential afforded by radial sampling, the use of MSE based protocols with acquisition times that are comparable to two-fold accelerated Cartesian MSE protocols, already yielded clinically feasible scan times, and more importantly made it possible to highlight the advantages of radial sampling given similar scan conditions.

Notwithstanding the good correlation between the T_2 maps produced by the EMC model-based reconstruction and the reference Cartesian values, this type of reconstruction is still challenging to optimize. This is mostly reflected in the sensitivity of the iterative procedure to the relative scaling between the fitted variables, affecting both convergence accuracy and speed [17]. In practice, we found the relative scaling to have lower significance when processing the phantom and brain T_2 maps, while having higher effect on the spinal-cord data. This is not unexpected, as the latter data is of *a priori* lower quality, and as such requires more careful tuning of the iterative reconstruction in order to accentuate signal changes pertaining to the encoded MR parameters as opposed to spurious motion-related perturbations and noise. Akin to the influence of regularization, a tradeoff was observed when choosing a suitable scaling value where excessive downscaling caused blurring, while insufficient downscaling failed to effectively remove noise. In practice, stable convergence was reached by identifying a ‘sweet-spot’ for each scaling-parameter value having a typical tolerance of ±20 % for the B_1 scaling and ±10 % for the T_2 scaling. These values were found empirically and employed in the post-processing of all acquired datasets.

The high quality of the radially sampled in vivo maps attests to the value of this sampling scheme, particularly in the spinal-cord region. These maps are, to the best of our knowledge, the first successful attempt at differentiating the T_2 values of the white- and gray-matter structures within the spinal cord. The sub-millimeter spatial resolution requirements for mapping these structures are, in this case, only met owing to the efficiency and motion robustness of radial sampling. Although it is difficult to estimate the motion-related blurring that occurs during in vivo scans (and therefore to state with confidence whether the prescribed resolution is actually reflected in the final maps) it is evident that the ensuing spatial definition is superior to what can be realized using Cartesian sampling, clearly illustrating the advantages of radial sampling in the face of irregular physiological motion. Further information regarding the influence of motion on radial sampling can be found in [10,38]. Investigation of its effect on the T_2 mapping accuracy is under way and will be reported in future publications.

Extending the iterative EMC model-based reconstruction to support other contrasts is feasible and the subject of ongoing work. A general requirement for accurate mapping is that the target MR parameters are sufficiently encoded during the signal acquisition process. This

can include the use of short TRs for increased T_1 weighting, implementation of variable refocusing flip-angles for improved B_1^+ encoding, or optimization of the echo spacing so as to sample both short and long echo-times in order to effectively encode multiple T_2 components. A generalized reconstruction framework can then be utilized to estimate multiple parameters jointly from a single acquisition, in a manner analogous to that used in the recently proposed MR fingerprinting technique [12]. In contrast to MR fingerprinting, which relies on incoherent aliasing artifacts in order to handle highly undersampled data, the EMC model-based approach incorporates information about the sampling trajectory directly into the signal model and tries to remove, rather than circumvent, the aliasing related artifacts. It can therefore handle both incoherent and coherent aliasing patterns, and support arbitrary k-space geometries. It should be noted that the EMC database computation time is expected to increase with each additionally encoded parameter. These calculations, however, are highly parallelizable and thus well suited for acceleration using multi-core processing units such as graphical processing units (GPUs).

CONCLUSIONS

This work demonstrates the feasibility of using radial sampling for rapid and robust mapping of T_2 relaxation in vivo. The combination of the EMC algorithm with model-based iterative reconstruction allows accurate extraction of the tissue T_2 values while removing the protocol- and parameter-dependent variability that impairs conventional exponential fitting. The ensuing acquisition and post-processing framework can be used for quantitative diagnosis of pathologies that require investigation of high-resolution structures embedded within larger tissue regions (e.g. the internal nuclei of the thalamus for direct targeting in functional neurosurgery), and of body regions affected by irregular physiological motion, such as the spinal-cord and prostate.

Acknowledgements

The authors would like to thank Dr. Ricardo Otazo for helpful discussions. This project was supported in part by NIH Grant R01 EB000447. DKS and NBE would like to acknowledge support from The Helen and Martin Kimmel Foundation for Innovative Research.

APPENDIX A

The derivatives of the EMC term in Eqs. (6)-(7) can be calculated numerically using the formal definition $df/dx = [f(x+h) - f(x)]/h$. Since the EMC function is defined at discrete T_2 values, its derivative with respect to an arbitrary value $T_{2,v}$ can be computed as the weighted average of the derivative above and below this value,

$$\frac{\partial EMC}{\partial T_{2,v}} \equiv \frac{1}{2}\left[\frac{EMC\left(T_{2,v}^{up}\right) - EMC\left(T_{2,v}\right)}{T_{2,v}^{up} - T_{2,v}} + \frac{EMC\left(T_{2,v}\right) - EMC\left(T_{2,v}^{down}\right)}{T_{2,v} - T_{2,v}^{down}}\right] \quad (9)$$

where $T_{2,v}^{up}$ and $T_{2,v}^{down}$ represent the neighboring EMC simulation points. An identical formalism can be then applied for the calculation of the derivative with respect to $B_{1,v}^+$ in Eq. (7).

APPENDIX B

Another practical aspect, attributed to the use of spatially specific regularization terms, was the ability to exclude low SNR regions from the reconstruction process, thereby focusing the reconstruction on targeted regions-of-interest and promoting faster convergence. To that end, an initial T_2-weighted estimate of the anatomy was generated via straightforward gridding of the entire dataset onto a Cartesian k-space grid, followed by Fourier transformation to the image domain. This image was normalized and then used to create a binary mask in which all regions with signal below a predefined threshold $\delta_{mask} = 0.1$ were set to zero. The resulting mask was finally applied in the Tikhonov terms of the cost function in Eq. (8) to exclude low SNR regions.

Abbreviations

RF	Radio Frequency
FOV	Field of View
ROI	Region of Interest
SNR	Signal-to-Noise Ratio
SE	Spin-Echo
MSE	Multi Spin-Echo
ETL	Echo-Train Length
EMC	Echo Modulation Curve
PD	Proton Density
B_1^+	Radiofrequency Transmit Field

REFERENCES

1. Siemonsen S, Mouridsen K, Holst B, Ries T, Finsterbusch J, Thomalla G, Ostergaard L, Fiehler J. Quantitative T2 values predict time from symptom onset in acute stroke patients. Stroke. 2009; 40(5):1612–16. [PubMed: 19325153]
2. Lund H, Jønsson A, Andersen J, Rostrup E, Paulson O, Sørensen P. Cognitive deficits in multiple sclerosis: correlations with T2 changes in normal appearing brain tissue. Acta Neurol Scand. 2012; 125(5):338–44. [PubMed: 21793807]
3. Cury R, Shash K, Nagurney J, Rosito G, Shapiro M, Nomura C, Abbara S, Bamberg F, Ferencik M, Schmidt E, Brown D, Hoffmann U, Brady T. Cardiac magnetic resonance with T2-weighted imaging improves detection of patients with acute coronary syndrome in the emergency department. Circulation. 2008; 118(8):837–44. [PubMed: 18678772]
4. Eitel I, Friedrich M. T2-weighted cardiovascular magnetic resonance in acute cardiac disease. J Cardiovasc Magn Reson. 2011; 13(1):13. [PubMed: 21332972]
5. Ptaszek L, Price E, Hu M, Yang P. Early diagnosis of hemochromatosis-related cardiomyopathy with magnetic resonance imaging. J Cardiovasc Magn Reson. 2005; 7(4):689–92. [PubMed: 16136860]
6. Liu W, Turkbey B, Sénégas J, Remmele S, Xu S, Kruecker J, Bernardo M, Wood B, Pinto P, Choyke P. Accelerated T2 mapping for characterization of prostate cancer. Magn Reson Med. 2011; 65(5):1400–6. [PubMed: 21394778]

7. Farraher S, Jara H, Chang K, Ozonoff A, Soto JA. Differentiation of hepatocellular carcinoma and hepatic metastasis from cysts and hemangiomas with calculated T2 relaxation times and the T1/T2 relaxation times ratio. J Magn Reson Imaging. 2006; 24(6):1333–41. [PubMed: 17083093]
8. Pan J, Pialat J, Joseph T, Kuo D, Joseph G, Nevitt M, Link T. Knee cartilage T2 characteristics and evolution in relation to morphologic abnormalities detected at 3-T MR imaging: a longitudinal study of the normal control cohort from the Osteoarthritis Initiative. Radiology. 2011; 261(2):507–15. [PubMed: 21900614]
9. Patten C, Meyer R, Fleckenstein J. T2 mapping of muscle. Semin Musculoskelet Radiol. 2003; 7(4): 297–305. [PubMed: 14735428]
10. Glover G, Pauly J. Projection reconstruction techniques for reduction of motion effects in MRI. Magn Recon Med. 1992; 28(2):275–89.
11. Doneva M, Börnert P, Eggers H, Stehning C, Sénégas J, Mertins A. Compressed sensing reconstruction for magnetic resonance parameter mapping. Magn Res Med. 2010; 64(4):1114–20.
12. Ma D, Gulani V, Seiberlich N, Liu K, Sunshine J, Duerk J, Griswold M. Magnetic resonance fingerprinting. Nature. 2013; 14(495)(7440):187–92. [PubMed: 23486058]
13. Block K, Uecker M, Frahm J. Model-based iterative reconstruction for radial fast spin-echo MRI. IEEE Trans Med Imaging. 2009; 28(11):1759–69. [PubMed: 19502124]
14. Altbach M, Outwater E, Trouard T, Krupinski E, Theilmann R, Stopeck A, Kono M, Gmitro A. Radial fast spin-echo method for T2-weighted imaging and T2 mapping of the liver. J Magn Reson Imag. 2002; 16(2):179–89.
15. Altbach M, Bilgin A, Li Z, Clarkson E, Trouard T, Gmitro A. Processing of radial fast spin-echo data for obtaining T2 estimates from a single k-space data set. Magn Res Med. 2005; 54(3):549–59.
16. Huang C, Graff C, Clarkson E, Bilgin A, Altbach M. T2 mapping from highly undersampled data by reconstruction of principal component coefficient maps using compressed sensing. Magn Reson Med. 2012; 67(5):1355–66. [PubMed: 22190358]
17. Huang C, Bilgin A, Barr T, Altbach M. T2 relaxometry with indirect echo compensation from highly undersampled data. Magn Reson Med. 2013; 70(4):1026–37. [PubMed: 23165796]
18. Lebel R, Wilman A. Transverse relaxometry with stimulated echo compensation. Magn Reson Med. 2010; 64(4):1005–14. [PubMed: 20564587]
19. Ben-Eliezer N, Sodickon DK, Block KT. Rapid and accurate T2 mapping from multi-spin-echo data using Bloch-simulation-based reconstruction. Magn Reson Med. 2014 doi: 10.1002/mrm.25156.
20. McKenzie C, Chen Z, Drost D, Prato F. Fast acquisition of quantitative T2 maps. Magn Reson Med. 1999; 41(1):208–12. [PubMed: 10025632]
21. Anderson S, Sakai O, Soto J, Jara H. Improved T2 mapping accuracy with dual-echo turbo spin echo: effect of phase encoding profile orders. Magn Reson Med. 2013; 69(1):137–43. [PubMed: 22374798]
22. Zur Y. An algorithm to calculate the NMR signal of a multi spin-echo sequence with relaxation and spin-diffusion. J Magn Reson. 2004; 171(1):97–106. [PubMed: 15504687]
23. Petrova M, Doktorov A, Lukzen N. CPMG echo amplitudes with arbitrary refocusing angle: explicit expressions, asymptotic behavior, approximations. J Magn Reson. 2011; 212(2):330–43. [PubMed: 21852166]
24. Prasloski T, Mädler B, Xiang Q, MacKay A, Jones C. Applications of stimulated echo correction to multicomponent T2 analysis. Magn Reson Med. 2012; 67(6):1803–14. [PubMed: 22012743]
25. Fernandez-Martineza JL, Pallerob JLG, Fernandez-Muniza Z, Pedruelo-Gonzaleza LM. The effect of noise and Tikhonov's regularization in inverse problems. Part II: The nonlinear case. J Appl Geophys. 2014 doi: 10.1016/j.jappgeo.2014.05.005.
26. Kim D, Jensen J, Wu E, Sheth S, Brittenham G. Breathhold multiecho fast spin-echo pulse sequence for accurate R2 measurement in the heart and liver. Magn Reson Med. 2009; 62(2):300–6. [PubMed: 19526516]
27. Smith S, Edden R, Farrell J, Barker P, Van Zijl P. Measurement of T1 and T2 in the cervical spinal cord at 3 tesla. Magn Reson Med. 2008; 60(1):213–9. [PubMed: 18581383]

28. Block K, Uecker M, Frahm J. Undersampled radial MRI with multiple coils. Iterative image reconstruction using a total variation constraint. Magn Reson Med. 2007; 57(6):1086–98. [PubMed: 17534903]

29. Hager W, Zhang H. A new conjugate gradient method with guaranteed descent and an efficient line search. Siam J Optim. 2005; 16(1):170–192.

30. Beatty P, Nishimura D, Pauly J. Rapid gridding reconstruction with a minimal oversampling ratio. IEEE Trans Med Imaging. 2005; 24(6):799–808. [PubMed: 15959939]

31. Nocedal, G.; Wright, S. Conjugate gradient methods, in Numerical optimization. Springer-Verlag; 1999.

32. Stanisz G, Odrobina E, Pun J, Escaravage M, Graham S, Bronskill M, Henkelman RM. T1, T2 relaxation and magnetization transfer in tissue at 3T. Magn Res Med. 2005; 54(3):507–12.

33. EMC based T2 mapping software package. Web address: http://cai2r.net/resources/software/emc-based-t2-mapping-package

34. Gold G, Han E, Stainsby J, Wright G, Brittain J, Beaulieu C. Musculoskeletal MRI at 3.0 T: relaxation times and image contrast. AJR Am J Roentgenol. 2004; 183(2):343–51. [PubMed: 15269023]

35. Jordan C, Saranathan M, Bangerter N, Hargreaves B, Gold G. Musculoskeletal MRI at 3.0 T and 7.0 T: a comparison of relaxation times and image contrast. Eur J Radiol. 2013; 82(5):734–9. [PubMed: 22172536]

36. Jezzard P, Duewell S, Balaban R. MR relaxation times in human brain: measurement at 4 T. Radiology. 1996; 199(3):773–9. [PubMed: 8638004]

37. Bieri O, Scheffler K, Welsch G, Trattnig S, Mamisch T, Ganter C. Quantitative mapping of T2 using partial spoiling. Magn Reson Med. 2011; 66(2):410–8. [PubMed: 21394766]

38. Chandarana H, Block K, Rosenkrantz A, Lim R, Kim D, Mossa D, Babb J, Kiefer B, Lee V. Free-breathing radial 3D fat-suppressed T1-weighted gradient echo sequence: a viable alternative for contrast-enhanced liver imaging in patients unable to suspend respiration. Invest Radiol. 2011; 46(10):648–53. [PubMed: 21577119]

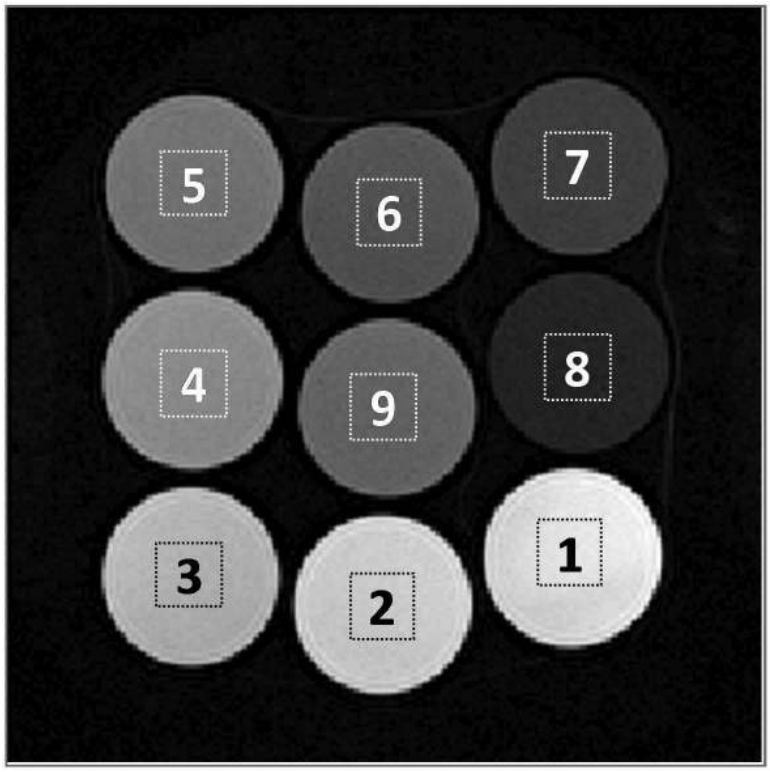

Figure 1.

T_2 weighted fast spin echo (**FSE**) image of the nine-tube phantom used in this study. Tubes [1...8] were doped with varying concentrations of manganese chloride ($MnCl_2$) imparting to each tube a different T_2 relaxation time. Tubes #9 and #5 were prepared with similar concentrations in order to verify the T_2 mapping consistency over different spatial locations.

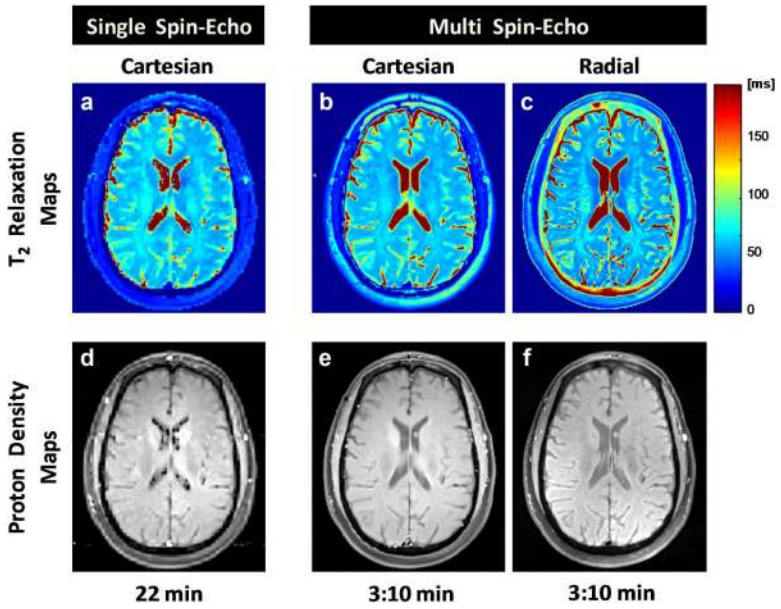

Figure 2.

In vivo T_2 and PD maps of a human brain in a healthy adult volunteer. (**a**) T_2 map derived from a single-SE dataset and fitted to an exponential decay curve of the form $S(t)=S_0\exp(-t/T_2)$. (**b**) T_2 map derived from a Cartesian multi SE (**MSE**) dataset via pixel-by-pixel matching of the experimental echo-modulation curve (**EMC**) to the database of simulated EMCs as proposed in [19]. (**d,e**) PD maps respectively matching the datasets in (a) and (b), derived by dividing the first echo-time (**TE**) image of each time-series by the decay factor predicted by the corresponding T_2 maps. (**c,f**) T_2 and PD maps, derived from a radially sampled dataset acquired during the same scan session. These maps were generated jointly using the EMC model-based iterative reconstruction introduced in this report.

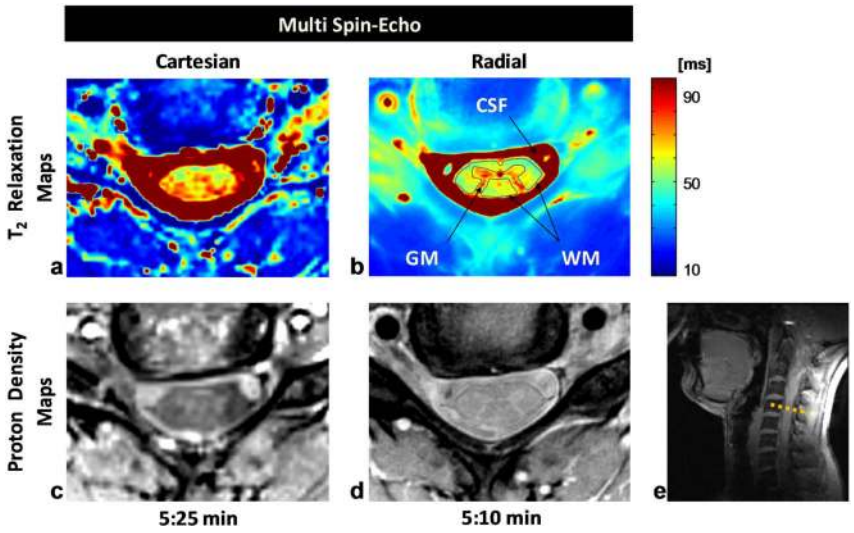

Figure 3.

In vivo T_2 and PD maps for an axial slice in the cervical spinal cord of a healthy adult volunteer. (**a**) T_2 map derived from a Cartesian MSE dataset via pixel-by-pixel matching of the experimental echo-modulation curve (**EMC**) to a database of simulated EMCs as proposed in [19]. (**c**) PD map, matching the dataset in (a) derived by dividing the first echo-time (TE) image of the time-series by the decay factor predicted by the corresponding T_2 map. (**b,d**) T_2 and PD maps, derived from a radially sampled dataset collected during the same scan session and utilizing the non-folding property of radial sampling to scan only half of the Cartesian FOV, thereby increasing the acquisition efficiency. Maps were generated jointly using the EMC model-based iterative reconstruction described in this report. (**e**) Reference T_1 weighted sagittal image, marking the location of the axial slice in (a-d) (yellow dotted line).

Table 1

Summary of the parameter values for all experiments described in this report.

		9-Tube Phantom			In vivo brain			In vivo spinal-cord	
Parameter	**Units**	**Single-SE Cartesian**	**Multi-SE Cartesian**	**Multi-SE Radial**	**Single-SE Cartesian**	**Multi-SE Cartesian**	**Multi-SE Radial**	**Multi-SE Cartesian**	**Multi-SE Radial**
TR	[ms]	1500	1500	1500	2000	2000	2000	2500	2500
TE	[ms]	12,24,...,216	12,24,...,216	12,24,...,216	15,30,...,90	10,20,...,220	12,24,...,228	13,26,...260	13,26,...,143
ETL		1	18	18	1	22	19	20	11
N_{EXC}		--	--	98	--	--	95	--	124
Matrix-size		192 × 192	192 × 192	--	128 × 108	192 × 162	--	128 X 128	--
Base resolution		192	192	192	128	192	192	128	240
FOV	[mm^2]	110 × 110	110 × 110	110 × 110	220 × 185	220 × 185	220 × 220	96 × 96	96 × 96
Slice-thickness*	[mm]	3	3	3	3	3	3	3	3
Refocusing angle	[deg]	90,120,150,180	90,120,150,180	90,120,150,180	180	180	180	180	180
BW_{acq}	[Hz/Px]	200	200	220	210	210	220	250	250
$N_{averages}$		1	1	2	1	1	1	1	1
Acceleration		None	None	3.1t	None	×2 GRAPPA	3.2†	None	3†
Total scan time	[h:mm:ss]	1:28:00	0:04:53	0:04:54	0:22:00	0:03:10	0:03:10	0:05:25	0:05:10

*Refocusing / excitation slice-thickness factor of 1.2 was used for all scans

†Radial acceleration = [(base-res × n/2) × ETL] / [N_{EXC} × ETL]

Table 2

$MnCl_2$ concentrations and corresponding T_2 values for the phantom shown in Figure 1.

			Cartesian	Radial Sampling				Cartesian Sampling							
Tube #	**$MnCl_2$ [mM]**	**T_1 [ms]**	**Single-SE T_2 Exponential fit [ms]**	**% Error in Multi-SE T2 EMC fit**				**% Error in Multi-SE T2 EMC fit**				**% Error in Multi-SE T2 Exponential fit**			
	$\alpha_{Refocus} \rightarrow$		**180°**	**180°**	**150°**	**120°**	**90°**	**180°**	**150°**	**120°**	**90°**	**180°**	**150°**	**120°**	**90°**
[1]	0.070	1424	116.7	5.3	0.5	1.4	4.9	0.9	1.1	3.9	5.9	35.6	42.2	59.4	99.3
[2]	0.135	877	68.5	2.5	6.0	7.3	8.6	3.6	3.8	5.5	9.1	33.7	39.4	53.4	85.1
[3]	0.270	528	36.9	1.7	7.9	7.9	11.1	1.6	2.7	4.9	7.9	40.1	46.1	68.6	110.0
[4]	0.405	363	23.5	2.2	7.7	6.8	11.5	0.0	0.4	3.0	6.4	45.1	54.5	74.0	132.8
[5]	0.540	235	17.9	1.8	5.0	0.6	1.1	0.0	1.7	3.9	11.7	53.1	79.3	97.2	182.1
[6]	0.675	214	14.4	2.2	9.7	6.9	12.5	1.4	0.0	2.1	8.3	56.3	74.3	88.9	172.2
[7]	0.800	155	11.9	8.6	10.1	9.2	4.2	0.8	0.8	6.7	11.8	67.2	82.4	106.7	213.4
[8]	1.000	120	9.7	7.8	7.2	6.2	10.3	4.1	8.2	13.4	8.2	71.1	51.5	112.4	230.9
[9]	0.540	287	17.8	2.3	9.0	8.4	12.9	1.1	1.1	2.2	6.2	52.2	71.9	83.1	143.3
			Mean % error:	**3.8**	**7.0**	**6.1**	**8.6**	**1.5**	**2.2**	**5.1**	**8.4**	**50.5**	**60.2**	**82.6**	**152.1**

T_2 values were obtained from either single-SE or multi-SE (**MSE**) pulse sequence for four different refocusing flip-angles. Radial data was post-processed using the EMC model-based reconstruction approach introduced in this report, while Cartesian data was post-processed using either an exponential fit (for single-SE) or the EMC algorithm described in [19] (for MSE). Percent errors of MSE T_2 fits relative to single-SE T_2 fits (calculated as the absolute difference between the single-SE and MSE values, divided by the reference single-SE values) for various sampling and fitting methods are reported in columns 5-17. Average relative errors are listed in the bottom row. The third column states the T_1 values of each test tube, reflecting a relatively constant T_1/T_2 ratio of 13.8 ± 1.3.